SIAM J. APPL. MATH.
Vol. 64, No. 6, pp. 2076–2095

ANALYTICAL SOLUTIONS OF A GROWTH MODEL FOR A MELT REGION INDUCED BY A FOCUSED LASER BEAM*

ANTOINE SAUCIER†, JEAN-YVES DEGORCE‡, AND MICHEL MEUNIER‡

Abstract. We consider processes in which a focused laser beam is used to induce the melting of silicium. The first goal of this paper is to propose a simple three-dimensional (3D) model of this melting process. Our model is partly based on an energy balance equation. This model leads to a nontrivial ODE describing the evolution in time of the dimension of the melt region. The second goal of this paper is to obtain approximate analytical solutions of this ODE. After using basic solution methods, we propose an original geometrical method to derive asymptotic solutions for time $\to \infty$. These solutions turn out to be the most useful for the description of this process.

Key words. focused laser beam, melting of material, three-dimensional (3D) modeling, ODE, analytic solution, asymptotic solution, geometrical method

AMS subject classifications. 34A05, 34A26, 34E10, 65L05, 74N20

DOI. 10.1137/S0036139902413015

1. Introduction.

Focusing an energetic pulsed photon beam on a material usually leads to a localized heating, possibly followed by atomic vaporization and even by an ejection of materials, a process called ablation [5]. All these mechanisms contribute to the dissipation of the laser beam energy into the materials. The time and spatial distribution of these dissipation phenomena depend on the localized heat source parameters and on the materials' properties. In this paper, we assume that the beam does not cause any ablation and that all the incoming energy is dissipated into heat, which leads to a local increase of temperature and to a melt region. The object of this study is the time evolution of the melt region size.

In general, these heating and melting effects constitute a three-dimensional (3D) heat flow problem usually solved numerically [4]. An analytical solution, even approximate, is very interesting because it allows analyzing the influence of the various physical parameters involved. Actually, simplifications to a one-dimensional (1D) heat flow problem have been proposed by many authors [9], [7], [6] for the case of a large beam dimension when compared to the heat diffusion length. However, for a long pulsed focused beam with beam dimension comparable to or smaller than the melt depth, the lateral heat flow is on the same order of magnitude as the perpendicular component. It follows that the 1D approximation is no longer valid. Nonlinear boundary conditions arising from a moving solid-liquid interface make exact analytical solutions of the 3D heat flow equation very difficult.

In this paper, we present a simplified 3D model based on an energy balance equation. This model was first introduced in [3] with a brief justification and with an emphasis on the comparison with experimental results. In this paper, our first goal is to present a *complete derivation* of this model (section 2), with an emphasis on the

*Received by the editors August 8, 2002; accepted for publication (in revised form) March 14, 2004; published electronically September 2, 2004.

http://www.siam.org/journals/siap/64-6/41301.html

†Department of Applied Mathematics and Industrial Engineering, École Polytechnique de Montréal, C.P. 6079, succ. centre-ville, Montréal, Québec, Canada, H3C-3A7 (Antoine.Saucier@polymtl.ca).

‡Laser Processing Laboratory, Department of Engineering Physics, École Polytechnique de Montréal, C.P. 6079, succ. centre-ville, Montréal, Québec, Canada, H3C-3A7 (jean-yves.degorce@polymtl.ca, meunier@email.phys.polymtl.ca).

nature of the approximations used. Our model leads to an ODE that describes the evolution in time of the dimension of the melt region for a material irradiated by a focused laser beam. The second goal of this paper is to obtain *approximate analytical solutions* of this ODE. In section 3, we analyze this ODE in detail using classical analytical and numerical methods. In sections 4 and 5, we derive asymptotic solutions for $t \to \infty$, using a possibly original geometrical method. Finally, in section 6, we compare the accuracy of the approximate solutions.

2. The model. Our model is based on four main hypotheses that we present and justify in the following.

2.1. Hypothesis A: The focused laser beam can be treated as a point heat source. In this paper, we assume that the laser beam is orthogonal to the flat material surface. A focused laser beam is most often characterized by a Gaussian curve of width r_0. The light intensity varies according to $I(r) = I_0 \ \exp(-(r/r_0)^2)$, where r is the distance from the beam center in a direction perpendicular to the beam. The heat diffusion characteristic length scale for a material of heat diffusivity D is usually defined by $d(t) = \sqrt{D\ t}$. $d(t)$ is an estimate of the heat front penetration depth at time t, assuming that the laser is turned on at $t = 0$.

A 1D model of the heating process is obtained if $r_0 >> d$. In this limit, the beam radius can be regarded as infinite. For an isotropic material, the resulting isothermals are planes which are perpendicular to the laser beam. If the beam is perpendicular to the flat material surface, then the isothermals are planes which are parallel to this surface.

A 3D model of the heating process is obtained if $r_0 << d(t)$. Photons entering a material are absorbed progressively. It follows that the light intensity within the material decreases according to an exponential law (Beers's law) characterized by a penetration depth ℓ (the inverse of the absorptivity). We develop our model of the heating process in the *point source approximation framework*, where both r_0 and ℓ are much smaller than the diffusion length, i.e.,

$$\begin{cases} r_0 << \sqrt{D\ t_{\rm p}} & \text{and} \\ \ell << \sqrt{D\ t_{\rm p}}, \end{cases} \tag{2.1}$$

where $t_{\rm p}$ is the pulse width and $d(t_{\rm p}) = \sqrt{D\ t_{\rm p}}$ is the diffusion length. We emphasize that the point source approximation (2.1) implies that our model is not expected to be valid or accurate for $t \approx 0$.

2.2. Hypothesis B: Heat losses at the surface of the melt domain are negligible during the whole melting process. Heat losses occur through two interfaces: the flat upper surface of the melt domain and the liquid-solid interface. In this section, we compare the magnitudes of these heat losses.

On one hand, it is a well-known experimental observation that the flat surface of the liquid domain has approximately the shape of a disk. On the other hand, the liquid-solid interface is a surface which is attached to the circumference of this disk. During the melting process, this surface is symmetric with respect to an axis going through the point heat source in the direction perpendicular to the solid-air plane. This symmetry implies that the area $\mathcal{A}$ of the liquid-solid interface can be expressed solely as a function of the disk radius r, i.e., $\mathcal{A} = \mathcal{A}(r)$. If we assume that the liquid-solid interface is not flat, then its area $\mathcal{A}(r)$ will be at least as large as

the area of the disk, i.e.,

$$\frac{\pi\ r^2}{\mathcal{A}(r)} \leq 1 \tag{2.2}$$

for $r > 0$.

Let us consider the ratio of the heat diffusion losses through these two surfaces. This ratio is $R = \frac{J_{\text{liquid/air}}}{J_{\text{liquid/solid}}}$, where $J_{\text{liquid/air}}$ and $J_{\text{liquid/solid}}$ are the heat fluxes through each interface. We use

$$\begin{cases} J_{\text{liquid/air}} &= \kappa_{\text{air}}\ \pi\ r^2 \quad \| \nabla T_{\text{air}} \|, \\ J_{\text{liquid/solid}} &= \kappa_{\text{solid}}\ \mathcal{A}(r) \quad \| \nabla T_{\text{solid}} \|, \end{cases} \tag{2.3}$$

where $(\kappa_{\text{air}}, \kappa_{\text{solid}})$ are the heat conductivities of the air and of the solid, respectively, and $(\| \nabla T_{\text{air}} \|, \| \nabla T_{\text{solid}} \|)$ are the magnitudes of the temperature gradients at the liquid surface in the air and in the solid, respectively. Using (2.3), the ratio R takes the form

$$R = \frac{\pi\ r^2}{\mathcal{A}(r)}\ \frac{\kappa_{\text{air}}}{\kappa_{\text{solid}}}\ \frac{\| \nabla T_{\text{air}} \|}{\| \nabla T_{\text{solid}} \|}. \tag{2.4}$$

If the solid and the air are at the same temperature initially, then we expect the temperature gradients at both interfaces to have similar magnitudes during the whole melting process, i.e., $\|\nabla T_{\text{air}}\| \approx \|\nabla T_{\text{solid}}\|$, and therefore $R \approx \frac{\pi\ r^2}{\mathcal{A}(r)}\ \frac{\kappa_{\text{air}}}{\kappa_{\text{solid}}}$. The inequality (2.2) then implies that R has an upper bound:

$$R \leq \frac{\kappa_{\text{air}}}{\kappa_{\text{solid}}}. \tag{2.5}$$

In general, the heat conductivity of gases is typically 100 times smaller than for solids, and therefore (2.5) implies that $R < 1/100$. Consequently, it seems reasonable to neglect heat losses in the air during the melting process. This kind of approximation has been discussed in the literature by Wood and Geist [8], who also took into account convection in the air and radiations.

2.3. Hypothesis C: The melt domain is hemispherical. We shall see that this hypothesis is essentially a consequence of the hypotheses A and B. We assume that the following three conditions are satisfied: the solid material is isotropic; the heat source is a point source (hypothesis A); the surface of the melt domain is effectively a thermal insulator (hypothesis B). It follows from these hypotheses that the temperature distribution has a *spherical symmetry*, i.e., that $T = T(r)$, where r is the distance from the point source.

The existence of a spherical symmetry can be understood by comparing our problem with another similar problem. Consider a point heat source within an *infinite* isotropic solid material, instead of a semi-infinite material. In this case, the temperature has obviously a spherical symmetry. Moreover, this symmetry implies that the heat flux going through an arbitrary plane containing the point heat source vanishes at each point of this plane. It follows that the problem with a spherical symmetry has exactly the same boundary condition (i.e., zero heat flux along a plane containing the source) as our problem in a semi-infinite material. For this reason, we expect the two problems to have the same symmetry.

Convective flow driven either by buoyancy or surface tension does not have enough time to develop for durations shorter than 1 μs, which is the laser pulse width in our application [1]. It follows that convection does not break the spherical symmetry.

Spherical symmetry implies that the isothermals are hemispherical. The liquid-solid interface, which is an isothermal, is therefore hemispherical.

2.4. Hypothesis D: Everything happens as if the heat flux at the surface of the melt region was transported instantaneously to the solid-liquid interface. In this section, we estimate the heat flux which crosses the liquid-solid interface. During a fixed time interval τ, the laser releases a constant quantity of energy which is absorbed at the top surface of the melt domain. This energy is used to heat the melt fluid, to melt a hemispherical shell of solid, and to heat the solid via diffusion. The thermal energy is transferred to the liquid-solid interface via conduction in the melt phase (convection being negligible).

In the framework of the Stefan problem [2], the energy density balance during a time lapse dt is evaluated at the moving liquid-solid interface (Figure 2.1):

$$j_{\text{in}}\ dt = j_{\text{out}}\ dt + L\ dr, \tag{2.6}$$

where j_{in} is the heat flux that reaches the interface inside the melt fluid, j_{out} is the heat flux diffused into the solid at the liquid-solid interface, and $L\ dr$ is the heat flux used to melt a region of solid of depth dr.

We integrate the energy balance equation (2.6) over the hemispherical shell of radius r and divide by dt to obtain the heat transfer rate balance

$$\int_{\text{interface}} j_{\text{in}}\ dS = j_{\text{out}}\ 2\pi r^2 + L\ \frac{dr}{dt}\ 2\pi r^2. \tag{2.7}$$

According to hypothesis B, we neglect heat losses in the air. It follows that the heat transfer rate $\int_{\text{interface}} j_{\text{in}}\ dS$ is the power provided by the laser (that we denote by P) minus the power used to heat the melt fluid (that we denote by $\frac{dE_{\text{h}}}{dt}$):

$$\int_{\text{interface}} j_{\text{in}}\ dS = P - \frac{dE_{\text{h}}}{dt}. \tag{2.8}$$

Substituting (2.8) into (2.7) yields

$$P = j_{\text{out}}\ 2\pi r^2 + L\ \frac{dr}{dt}\ 2\pi r^2 + \frac{dE_{\text{h}}}{dt}. \tag{2.9}$$

We approximate j_{out} by the linearization

$$j_{\text{out}} = -\kappa_{\text{s}}\ \left(\frac{\partial T}{\partial r}\right)_{r=r_{\text{m}}} \approx \frac{\kappa_{\text{s}}\ \Delta_{\text{s}}T}{\xi\sqrt{D\ t}}, \tag{2.10}$$

where κ_{s} is heat conductivity of the solid phase, r_{m} is the radius of the melt region, $\Delta_{\text{s}}T \equiv T_{\text{m}} - T_{\text{s}}$, T_{m} and T_{s} are the silicium fusion temperature and the solid silicium temperature far from the melt region, respectively (T_{s} equals the room temperature T_{room}), D is the thermal diffusivity in the solid at the fusion temperature T_{m}, $\sqrt{D\ t}$ is the heat diffusion characteristic length scale of the solid, and ξ is a geometry dependent constant usually fixed to 1.

The energy used to heat a hemisphere of melt solid satisfies

$$\frac{dE_h}{dt} = c_\ell\ \frac{2}{3}\ \pi\ r^3\ \frac{dT_\ell}{dt}, \tag{2.11}$$

where c_ℓ is the liquid silicium specific heat and T_ℓ is the mean temperature of the liquid silicium.

Substituting (2.10) and (2.11) into (2.9) leads to the energy transfer rate balance equation

$$P = \frac{\kappa_{\mathrm{s}}\ \Delta_{\mathrm{s}}T}{\xi\sqrt{D\ t}}\ 2\pi r^2 + L\ \frac{dr}{dt}\ 2\pi r^2 + c_\ell\ \frac{2}{3}\ \pi\ r^3\ \frac{dT_\ell}{dt}. \tag{2.12}$$

We will now compare the magnitude of the three terms

$$\begin{cases} P_{\mathrm{diffusion}} = \frac{\kappa_{\mathrm{s}}\ \Delta_{\mathrm{s}}T}{\xi\sqrt{D\ t}}\ 2\ \pi\ r^2, \\ P_{\mathrm{melting}} = L\ \frac{dr}{dt}\ 2\ \pi\ r^2, \\ P_{\mathrm{liquid\ heating}} = c_\ell\ \frac{2}{3}\ \pi\ r^3\ \frac{dT_\ell}{dt}. \end{cases} \tag{2.13}$$

In the second and third equations of (2.13), the instantaneous rates $\frac{dr}{dt}$ and $\frac{dT_\ell}{dt}$ are unknown a priori. However, the average rates can be estimated. For a time lapse τ, the average rates are defined by $\frac{dr}{dt}|_{\mathrm{mean}} = r/\tau$ and $\frac{dT_\ell}{dt}|_{\mathrm{mean}} = \frac{\Delta_\ell T}{\tau}$. In this problem, the laser beam power is constant and the size of the melt pool grows with time. Because the volume to heat increases as time passes, we expect both dr/dt and dT_ℓ/dt to decrease with time, i.e., to have negative second derivatives. This implies that *the average rates are larger than the instantaneous rates*. Substituting the average rates into (2.13) yields

$$\begin{cases} P_{\mathrm{diffusion}} = \frac{\kappa_{\mathrm{s}}\ \Delta_{\mathrm{s}}T}{\xi\sqrt{D\ t}}\ 2\ \pi\ r^2, \\ P_{\mathrm{melting}} \le L\ \frac{r}{\tau}\ 2\ \pi\ r^2, \\ P_{\mathrm{liquid\ heating}} \le c_\ell\ \frac{2}{3}\ \pi\ r^3\ \frac{\Delta_\ell T}{\tau}. \end{cases} \tag{2.14}$$

We use parameter values which are close to the ones observed experimentally for a focused laser beam on silicium, i.e., $r = 1\ \mu$m, $D = 0.1\ \mathrm{cm}^2/\mathrm{s}$, $\kappa_{\mathrm{s}} = 0.3\ \mathrm{W}/(\mathrm{cm}\ ^\circ\mathrm{K})$, $\Delta_\ell T = T_{\mathrm{vapor(Si)}} - T_{\mathrm{melt(Si)}} = 900\ ^\circ$K (by using the vaporization temperature of silicium, we overestimate $P_{\mathrm{liquid\ heating}}$), $\Delta_{\mathrm{s}}T = T_{\mathrm{melt(Si)}} - T_{\mathrm{room}} = 1400\ ^\circ$K, $c_{\mathrm{l}} = 0.91\ \mathrm{J}/(\mathrm{g}\ ^\circ\mathrm{K})$, $\tau = 1\ \mu$s, and $L = 4129\ \mathrm{J}/(\mathrm{cm}^3)$. Equation (2.14) leads to

$$\begin{cases} P_{\mathrm{diffusion}} = 0.083\ \mathrm{W}, \\ P_{\mathrm{melting}} \le 0.025\ \mathrm{W}, \\ P_{\mathrm{liquid\ heating}} \le 0.0017\ \mathrm{W}. \end{cases} \tag{2.15}$$

For short times, i.e., $t \le t_{\mathrm{p}}$, we expect both $r(t)$ and $T_\ell(t)$ to increase rapidly with time and consequently the instantaneous rates dr/dt and dT_ℓ/dt should be close to their average values. It follows that we can use the upper bounds in the second and third lines of (2.15) as estimates of P_{melting} and $P_{\mathrm{liquid\ heating}}$, which leads to $P_{\mathrm{melting}}/P_{\mathrm{liquid\ heating}} \approx 15$. $P_{\mathrm{liquid\ heating}}$ is therefore the smallest contribution to the energy balance, which is dominated by $P_{\mathrm{diffusion}}$ and P_{melting}. Combining the latter two contributions, we get

$$\frac{P_{\mathrm{liquid\ heating}}}{P_{\mathrm{diffusion}} + P_{\mathrm{melting}}} < \frac{2}{100}. \tag{2.16}$$

The energy stored by the heating fluid is therefore quite small compared to the energy transported by conduction and the energy used to melt the solid. In the following, we make the hypothesis that $P_{\mathrm{liquid\ heating}}$ can be neglected. It follows that the energy transferred by the laser during consecutive equal length time intervals can be regarded

as an *incompressible train* of equal size energy grains. Since the energy used to heat the fluid is negligible, then for each grain of energy entering the fluid at the upper surface, there is another grain of energy (emitted earlier) that exits the fluid at the liquid-solid interface. In other words, everything happens *as if* the energy entering the liquid at the top surface was transported instantaneously at the liquid-solid interface.

2.5. Derivation of the ODE based on the model hypotheses. According to hypothesis C, the melt region can be described by a hemisphere of radius r, as shown in Figure 2.1. We will therefore focus on the description of $r(t)$ as a function of the time t. According to the point heat source hypothesis A, the condition of validity of our model is

$$r(t) >> r_0, \tag{2.17}$$

where r_0 is the beam radius.

According to hypothesis D, we neglect the third term of (2.12) (on the right-hand side) to obtain

$$P = \frac{\kappa_s \, \Delta_s T}{\xi \sqrt{D \, t}} \, 2\pi r^2 + L \, 2\pi r^2 \, \frac{dr}{dt}. \tag{2.18}$$

Introducing the dimensionless quantities

$$x \equiv \, 2 \, \pi \, \frac{r}{r_0}, \quad \tau = 4 \, \pi^2 \, \frac{D \, t}{r_0^2}, \quad p = \frac{P}{D \, L \, r_0}, \tag{2.19}$$

we can rewrite (2.18) in the equivalent form

$$\frac{dx}{d\tau} = \frac{p}{x^2} - \frac{A}{\tau^{1/2}}, \tag{2.20}$$

where we introduce the dimensionless material-properties-only constant

$$A \equiv \frac{\kappa_s \, \Delta_s T}{\xi \, D \, L}. \tag{2.21}$$

For most materials, $A \approx 1$. With typical values for D (0.1 cm^2/s), L (4129 J/cm^3), $\Delta_s T$ (1400 K), r_0 (10^{-4} cm), and $P = 1$ W, we get $\tau \approx 4 \times 10^8 \, t$ and $p \approx 25$. Using the first quantity in (2.19), the constraint (2.17) implies that $x >> 2\pi$.

2.6. Initial value. The laser beam is turned on at $\tau = 0$ and is kept on afterward. The size of the melt region is zero at $\tau = 0$, and therefore it seems natural to use the initial value $x(0) \equiv x_0 = 0$. However, the differential equation (2.20) happens to be *singular* at $\tau = 0$ and $x = 0$. These singularities deserve a few comments.

First, we should stress that according to hypothesis A (point source approximation), we do not expect our model to be valid for $r = 0$. Indeed, the assumption (2.1) implies that $r(t) >> r_0$ and $t >> \frac{r_0^2}{D}$. Let us nevertheless consider our model in the limit $r \to 0$ and $t \to 0$.

The origin of the singularity at $t = 0$ is the term $\frac{\kappa_s \, \Delta_s T}{\xi \sqrt{D \, t}} \, 2\pi r^2$ in (2.18). The parameter $\Delta_s T \equiv T_m - T_{room}$ is fixed in our model, whereas in reality $\Delta_s T = 0$ for $t = 0$. Indeed, the medium does not melt instantaneously and therefore the temperature at the laser beam impact point increases rapidly from its initial value T_{room} to reach the melt value T_m. As expected, our equation does not correctly model this part of the heating process, which causes the singularity at time zero.

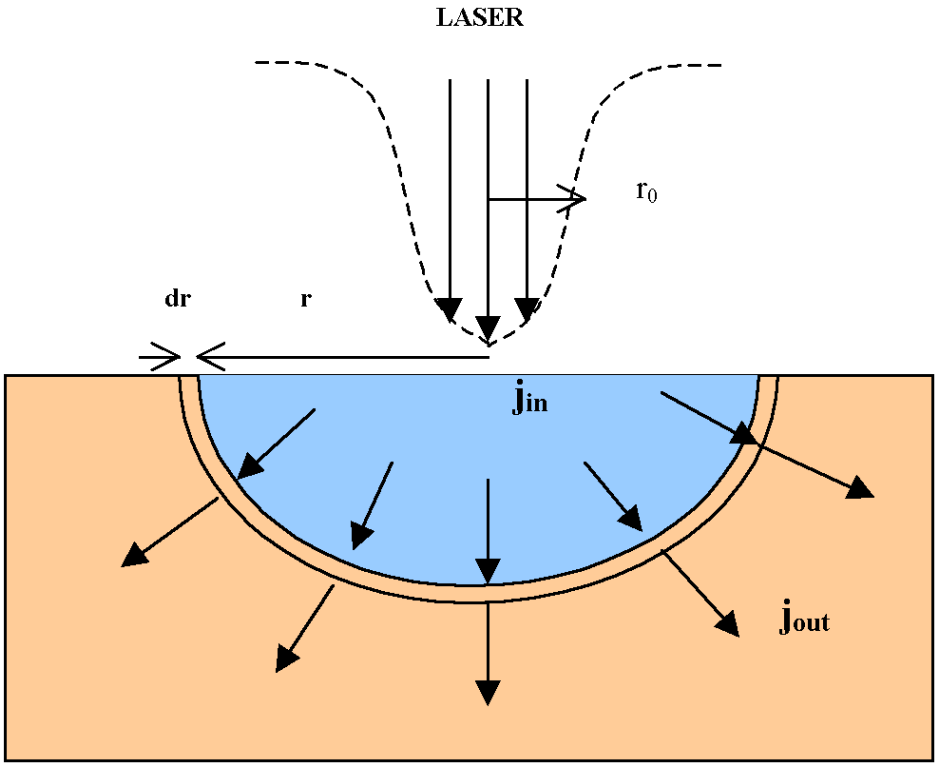

FIG. 2.1. *Schematics showing the hemispherical melt region of a semiconductor irradiated by a focused beam.*

The singularity at $r = 0$ is more physical because we expect $\frac{dr}{dt}$ to be very large for $t \approx 0$. Indeed, for $t \approx 0$ the finite power from the laser beam is transferred to a tiny hemisphere, which naturally causes the material to melt rapidly and consequently $\frac{dr}{dt}$ to be very large. In numerical simulations, we have to consider initial values such that $r_0 > 0$, even if it is not consistent with the physics of the problem. As a compromise, we will consider solutions with $r_0 > 0$ in the limit $r_0 \to 0^+$.

2.7. A preliminary simplification of the ODE. The change of variables

$$R = p^{-1}\, x \quad , \quad \theta = p^{-2}\, \tau \tag{2.22}$$

transforms (2.20) into

$$\frac{dR}{d\theta} = f(R,\theta) \equiv \frac{1}{R^2} - \frac{A}{\sqrt{\theta}}, \tag{2.23}$$

which contains only one parameter (i.e., $A \geq 0$), instead of two (i.e., A and p). In the following, we will study the ODE (2.23) with the initial condition $R(0) \equiv R_0 > 0$. The restriction $x >> 2\pi$ implies that $R >> 0.25$ (i.e., $R >> 2\pi/p$ with $p = 25$). According to (2.22), the solutions of (2.20) and (2.23) are directly related by $x(\tau, x_0) = p\ R(p^{-2}\tau, R_0)$. If $R_0 = x_0 \approx 0$, then

$$x(\tau) = p\ R(p^{-2}\tau). \tag{2.24}$$

In the following, we will assess the accuracy of approximate analytical solutions by comparison with numerical solutions, for which we use $A = 0.75$, which is the value of A corresponding to silicium.

3. Basic considerations.

3.1. Separability and integrating factor. Equation (2.23) is a nonlinear first order nonautonomous ODE. If $A = 0$, then (2.23) becomes $\frac{dR}{d\theta} = \frac{1}{R^2}$, which is *separable*, and the solution is

$$R(\theta) = (3\,\theta + R_0^3)^{1/3}. \tag{3.1}$$

However, if $A > 0$, then (2.23) is *not separable*. Moreover, an integrating factor that depends only on R or only on θ does not exist.

3.2. Sign of the derivative and direction field. Equation (2.23) can be rewritten in the equivalent form

$$\frac{dR}{d\theta} = -\frac{A}{R^2\sqrt{\theta}}\left(R + \frac{\theta^{1/4}}{\sqrt{A}}\right)\left(R - \frac{\theta^{1/4}}{\sqrt{A}}\right), \tag{3.2}$$

which shows that the function

$$\rho_0(\theta) \equiv \frac{\theta^{1/4}}{\sqrt{A}} \tag{3.3}$$

plays a special role. On one hand, $\rho_0(\theta)$ satisfies $f(\rho_0(\theta), \theta) = 0$. On the other hand, it follows from (3.2) that

$$\begin{cases} dR/d\theta < 0 & \text{if} \quad R > \rho_0(\theta), \\ dR/d\theta > 0 & \text{if} \quad R < \rho_0(\theta). \end{cases} \tag{3.4}$$

The inequalities (3.4) suggest that orbits have a tendency to remain close to $\rho_0(\theta)$, i.e., that $\rho_0(\theta)$ *is an asymptotic solution* for $\theta \to \infty$. This is indeed the case, in the sense that $\dot{\rho}_0(\theta) - f(\rho_0(\theta), \theta) = \frac{\theta^{-3/4}}{4\sqrt{A}} \to 0$ as $\theta \to \infty$. The *direction field* (DF) of (2.23) was plotted in Figure 3.1 for $A = 0.75$ and $0 \le \theta \le 1$. The DF is *horizontal* on the solid curve $R = \rho_0(\theta)$. The DF is pointing downward along the R-axis, which indicates that orbits dive down for $\theta \approx 0$ and $R(0) > 0$. However, the large θ behavior of the field is consistent with an increasing $R(\theta)$ as θ increases.

3.3. Singularities and numerical solutions. Equation (2.23) is *singular* at $R = 0$ and $\theta = 0$, which is problematic for initial values of the form $R(0) = R_0 > 0$. The singularity at $\theta = 0$ can be circumvented with the change of variable $s = \sqrt{\theta}$, which transforms (2.23) into

$$\frac{dR}{ds} = 2\left(-A + \frac{s}{R^2}\right). \tag{3.5}$$

Equation (3.5) is no longer singular at $s = 0$ but remains singular at $R = 0$. We obtained our numerical solutions[1] by solving (3.5) and then by replacing s by $\sqrt{\theta}$. With this method, we obtained several numerical solutions corresponding to different values of $R_0 > 0$ (Figure 3.2).

[1] In this paper, numerical solutions were obtained with the *Mathematica* function NDSolve, which switches between a nonstiff Adams method and a stiff Gear method.

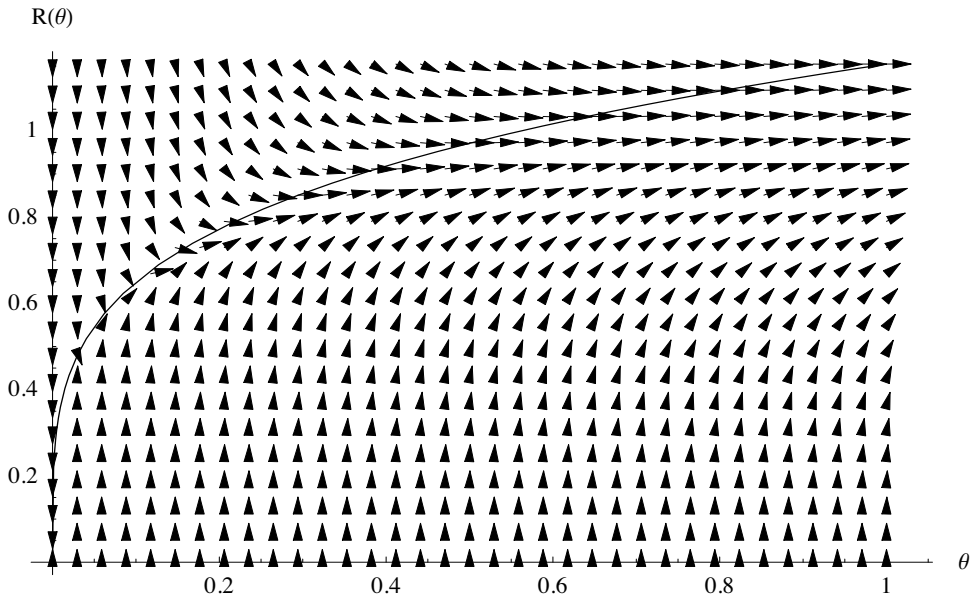

FIG. 3.1. *DF of* (2.23) *for* $A = 0.75$. *The solid curve represents the set of points for which the DF is horizontal, i.e.,* $R = \rho_0(\theta) \equiv \theta^{1/4}/\sqrt{A}$.

Considering Figure 3.2, the first important observation is that $R(\theta, R_0)$ is virtually independent of R_0 for large enough θ. This is fortunate because we did not know a priori which value to choose for R_0. Figure 3.2 informs us that any $R_0 < 0.1$ leads essentially to the same solution for $\theta >> 0.002$. The second observation is that the validity condition $R >> 0.25$ corresponds approximately to the *validity range* $\theta >> \theta_1 \equiv 0.002$.

3.4. Anomalous behavior of $R(\theta)$ around $\theta = 0$. The physics of this problem implies that the melt region expands with time. However, as clearly seen on the DF, all solutions with $R_0 > 0$ dive down in the neighborhood of $\theta = 0$ before eventually going up again. This peculiar behavior occurs in the region where the ODE is not valid. To be cautious, it is important to see if this anomaly can overlap the validity range $\theta > \theta_1$ of the ODE.

We analyzed the behavior of $R(\theta)$ as $\theta \to 0$ in Appendix A and found that

$$\begin{cases} \text{If } R_0 > 0, \ R(\theta) \sim R_0 - 2\ A\ \sqrt{\theta} + \frac{1}{R_0^2}\ \theta, \\ \text{If } R_0 \approx 0, \quad R(\theta) \sim (3\ \theta)^{1/3} \end{cases} \tag{3.6}$$

as $\theta \to 0$. Solutions with $R_0 > 0$ and $R_0 \approx 0$ are qualitatively different. Indeed, if $R_0 \approx 0$, then $R(\theta)$ *increases* for all $\theta \geq 0$, as it should. However, if $R_0 > 0$, then $R(\theta)$ *decreases*, reaches a minimum around $\theta_{\min} = A^2\ R_0^4$, and then increases ($R(\theta)$ is U-shaped). If we consider, for instance, a solution obtained with $R_0 = 0.001$, then we get $\theta_{\min} \approx 5.6 \times 10^{-13} << \theta_1 = 0.002$. Hence the anomalous behavior (3.6) occurs at very short times and does not overlap the validity range $\theta > \theta_1$ of the ODE.

3.5. Perturbation solution for A small. The solution for $A = 0$ is known exactly, i.e., $R(\theta) = (R_0^3 + 3\ \theta)^{1/3}$, and we assume that $0 \leq A \leq 1$. In this context, it is appropriate to look for a perturbation solution that would be valid for A small. If

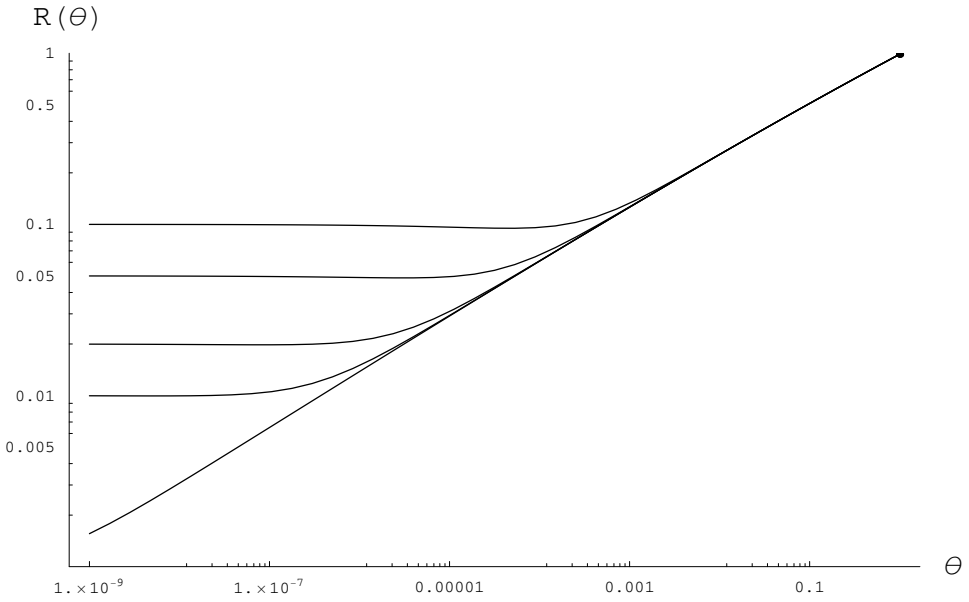

FIG. 3.2. *Numerical solutions for the initial values* $R(0) = (0.001, 0.01, 0.02, 0.05, 0.1)$.

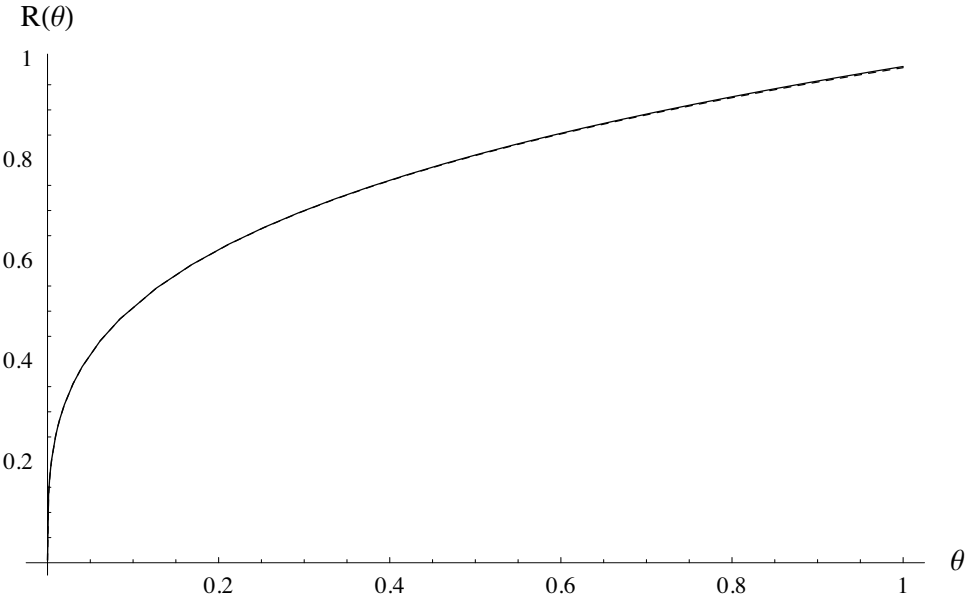

FIG. 3.3. *The solid curve is a numerical solution with* $R(0) = 0.001$ *and* $A = 0.75$*, while the dotted curve is the perturbation solution* (3.8)*. The curves are superposed; i.e., the agreement is excellent.*

we search for a solution of the form

$$R(\theta) = \sum_{n=0}^{\infty} A^n \; R_n(\theta), \tag{3.7}$$

where the R_ns are unknown functions and $R(0) = 0$, then it is straightforward to show (see Appendix B) that the perturbation method leads to the series

$$R(\theta) = (3\ \theta)^{1/3} - \frac{6}{7}\ \sqrt{\theta}\ A + \frac{3}{49}\ (3\ \theta)^{2/3}\ A^2 - \frac{8\ 3^{1/3}}{343}\ \theta^{5/6}\ A^3 - \frac{711}{12005}\ \theta\ A^4 + \frac{4824\ 3^{2/3}}{924385}\ \theta^{7/6}\ A^5 + O(A)^6. \tag{3.8}$$

As shown in Figure 3.3, an excellent agreement of (3.8) with numerical solutions is obtained for $0 \leq \theta \leq 1$.

3.6. Dependence of the solution on the parameter A. We notice that (3.8) can be written in the form $R(\theta) = \sum_{n=0}^{5} c_n\ (\theta^{1/6})^{n+2}\ A^n$, where the c_ns are real coefficients. Factorizing $\theta^{1/3}$ yields $R(\theta) = \theta^{1/3}\ \sum_{n=0}^{5} c_n\ (A\ \theta^{1/6})^n$, which suggests that the solution with $R_0 = 0$ has the general form

$$R(\theta) = \theta^{1/3}\ F(A\ \theta^{1/6}), \tag{3.9}$$

where F is an unknown function. Substituting (3.9) into (2.23) and using the change of variable $u = A\ \theta^{1/6}$ lead to

$$\frac{dF}{du} = \frac{6\ (1 - u\ F^2) - 2\ F^3}{u\ F^2}. \tag{3.10}$$

Equation (3.10) does not depend explicitly on A, and therefore (3.9) is indeed correct in general. The initial condition for (3.10) is $F(0) = 3^{1/3}$, which follows from $R(\theta) \sim (3\ \theta)^{1/3}$ as $\theta \to 0$. Equation (3.10) is a *key equation* that allows us to recover the MacLaurin series of $F(u)$ directly, i.e., without using the perturbation method. Consider, for instance, $F'(0)$. According to (3.10), $F'(0)$ has an indeterminate form $0/0$. However, using l'Hôspital's rule yields $F'(0) = \lim_{u\to 0} \frac{-6\ (F^2 + 2\ u\ F\ F') - 6\ F^2\ F'}{F^2 + 2\ u\ F\ F'} = -6 - 6\ F'(0) \Rightarrow F'(0) = -6/7$, which is correct according to (3.8). Higher order derivatives can also be obtained to recover the whole expansion, i.e., $F(u) = 3^{1/3} - \frac{6}{7}\ u + \frac{9\ 3^{2/3}}{49}\ u^2 - \frac{8\ 3^{1/3}}{343}\ u^3 - \frac{711}{12005}\ u^4 + \frac{4824\ 3^{2/3}}{924385}\ u^5 + O(u)^6$.

4. Asymptotic behavior for $\theta \to \infty$. In the spirit of the geometrical methods of Poincaré, we will try to locate the orbit $R(\theta)$ by examining its distance with respect to a reference curve. We have seen previously that the curve $R = \rho_0(\theta)$, defined by (3.3), is an asymptotic solution as $\theta \to \infty$. We will therefore choose $R = \rho_0(\theta)$ as our reference curve. We consider the time evolution of the distance function $U(\theta)$ defined by

$$U(\theta) \equiv \frac{1}{2}\left(R(\theta) - \rho_0(\theta)\right)^2. \tag{4.1}$$

A time derivative gives $\frac{dU}{d\theta} = (R - \rho_0)(\dot{R} - \dot{\rho}_0) = (R - \rho_0)(f(R,\theta) - \dot{\rho}_0)$. The factor $f(R,\theta) - \dot{\rho}_0$ has two roots $R = \pm\ \rho_1(\theta)$, which yields the factorization

$$\frac{dU}{d\theta} = -\ \frac{(1 + 4\ A^{3/2}\ \theta^{1/4})}{4\ \sqrt{A}\ R^2\ \theta^{3/4}}\ (R + \rho_1(\theta))(R - \rho_0(\theta))(R - \rho_1(\theta)), \tag{4.2}$$

where

$$\rho_1(\theta) = \frac{2\ A^{1/4}\ \theta^{3/8}}{\sqrt{1 + 4\ A^{3/2}\ \theta^{1/4}}}. \tag{4.3}$$

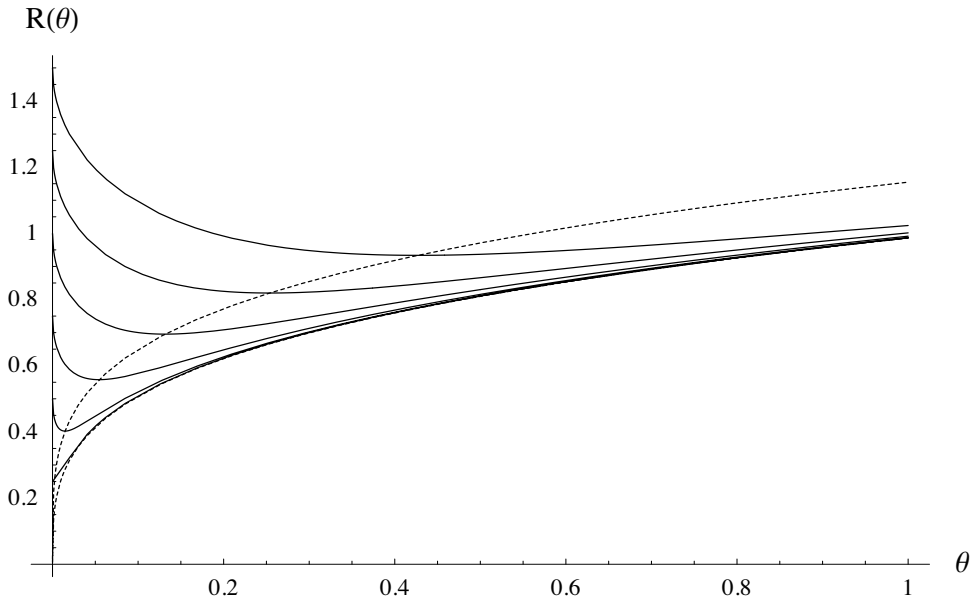

FIG. 4.1. *Dotted lines: Functions $\rho_0(\theta)$ (top) and $\rho_1(\theta)$ (bottom). Solid lines are orbits with different values of $R(0) > 0$, i.e., $(0.01, 0.1, 0.25, 0.5, 0.75, 1, 1.25, 1.5)$. The solutions that correspond to $R(0) = 0.01$ and 0.01 are superposed. Here $A = 0.75$.*

The functions $\rho_0(\theta)$ and $\rho_1(\theta)$, which are plotted in Figure 4.1 for $A = 0.75$, satisfy

$$\rho_0(\theta) > \rho_1(\theta) > 0 \tag{4.4}$$

for all $\theta > 0$ as long as $A > 0$. It follows from (4.2) and (4.4) that

$$\begin{cases} \frac{dU}{d\theta} < 0 & \text{if} \quad R > \rho_0(\theta) \ \text{ or } \ R < \rho_1(\theta), \\ \frac{dU}{d\theta} > 0 & \text{if} \quad \rho_0(\theta) < R < \rho_1(\theta), \\ \frac{dU}{d\theta} = 0 & \text{if} \quad R = \rho_0(\theta) \text{ or } R = \rho_1(\theta). \end{cases} \tag{4.5}$$

In other words, the *crescent-shaped zone* bounded by the curves $R = \rho_0(\theta)$ and $R = \rho_1(\theta)$ is *attractive* for all orbits that are outside the crescent. If $R(0) > 0$, then the orbit is in the region $R > \rho_0(\theta)$ initially, i.e., outside the crescent. If $R(0) = 0$, then according to (3.6) we have $R(\theta) \sim (3\ \theta)^{1/3}$ as $\theta \to 0$, and consequently the orbit lies between the two curves $\rho_0(\theta)$ and $\rho_1(\theta)$ initially. Indeed, $\rho_1(\theta) \sim 2\ A^{1/4}\ \theta^{3/8}$ as $\theta \to 0$, and one shows easily that $2\ A^{1/4}\ \theta^{3/8} < (3\ \theta)^{1/3} < \theta^{1/4}/\sqrt{A}$ as $\theta \to 0$. In summary, the orbit is initially located either *above* the reference curve $R = \rho_0(\theta)$ (for $R_0 > 0$), or *between* $\rho_0(\theta)$ and $\rho_1(\theta)$ (for $R_0 = 0$).

If the orbit starts *above* $R = \rho_0(\theta)$, then it follows from the first line of (4.5) that $R(\theta)$ gets closer to $\rho_0(\theta)$ as θ increases. This behavior is illustrated by the numerical solutions displayed in Figure 4.1. All orbits with $R(0) > 0$ *cross* the curve $R = \rho_0(\theta)$ because the DF is horizontal on this curve. Once inside the *crescent-shaped* region $\rho_0(\theta) < R < \rho_1(\theta)$, then the second line of (4.5) implies that the orbit $R(\theta)$ *goes away* from the upper boundary of the crescent $R = \rho_0(\theta)$. We are going to prove that this orbit *cannot cross the bottom curve* $R = \rho_1(\theta)$ because this would imply $\dot{U}(\theta) > 0$, which is not possible *on* and *below* this curve according to (4.5).

First,

$$\dot{U} = (\rho_0 - R)(\dot{\rho}_0 - \dot{R}) = (\rho_0 - R)\ \dot{D}, \tag{4.6}$$

where $D(\theta) \equiv \rho_0(\theta) - R(\theta)$. The distance $D(\theta)$ satisfies

$$\dot{D} = \dot{\rho}_0(\theta) - \dot{R}(\theta) = \dot{\rho}_0(\theta) - \dot{\rho}_1(\theta) + \dot{\rho}_1(\theta) - \dot{R}(\theta) = \dot{D}_0 + \dot{\rho}_1(\theta) - \dot{R}(\theta), \tag{4.7}$$

where $D_0(\theta) \equiv \rho_0(\theta) - \rho_1(\theta)$ is the distance between the two curves. It can be shown that $\dot{D}_0 > 0$ for all $\theta > 0$; i.e., the distance separating the two curves increases. If we assume that an orbit crosses the curve $R = \rho_1(\theta)$ *from above*, then this orbit has to satisfy $\dot{R} < \dot{\rho}_1 \Rightarrow \dot{\rho}_1(\theta) - \dot{R}(\theta) > 0$ *at the crossing point*. Since $\dot{D}_0 > 0$ and $\dot{\rho}_1(\theta) - \dot{R}(\theta) > 0$ at the crossing point, (4.7) implies that $\dot{D} > 0$. Since $R < \rho_0$ and $\dot{D} > 0$ at the crossing point, it follows from (4.6) that $\dot{U} > 0$, which is not possible *on* or *below* the curve $R = \rho_1(\theta)$ according to (4.5). Hence there is no crossing point.

The orbit *must therefore remain within the crescent*, while going away from the upper curve $R = \rho_0(\theta)$. Orbits that start *within the crescent*, and, in particular, the orbit with $R_0 = 0$, also remain within the crescent for all $\theta > 0$ (for the same reasons). It can be shown that $\lim_{\theta\to\infty} \rho_0(\theta) - \rho_1(\theta) = 1/(8\ A^2)$. Hence the orbit is *sandwiched between two curves that are separated by an asymptotically finite constant distance* and goes away from the upper curve. Numerical solutions (Figure 4.1) indicate that the limit orbit is much closer to $\rho_1(\theta)$ (bottom curve) than to $\rho_0(\theta)$ for $A = 0.75$. It follows that a possible asymptotic behavior for the orbit is

$$R(\theta) \sim \frac{2\ A^{1/4}\ \theta^{3/8}}{\sqrt{1 + 4\ A^{3/2}\ \theta^{1/4}}}\ +\ \mathrm{C}(A, R_0)\ \ \text{as}\ \ \theta \to \infty, \tag{4.8}$$

where $\mathrm{C}(A, R_0) << 1/(8\ A^2)$. Numerical solutions suggest that $\mathrm{C}(A, R_0)$ could be independent of R_0. $\rho_1(\theta)$ satisfies (2.23) asymptotically as $\theta \to \infty$. Indeed, as $\theta \to \infty$, we have $\dot{\rho}_1(\theta) - f(\rho_1(\theta), \theta) \sim \frac{1}{4\sqrt{A}\ \theta^{3/4}} \to 0$. Finally, let us stress that (4.8) has exactly the functional form (3.9), with $F(u) = (2\ u^{1/4})/(\sqrt{1 + 4\ u^{3/2}})$.

5. More accurate asymptotic solutions for $\theta \to \infty$. The asymptotic solution $\rho_1(\theta)$ was shown to be an improvement on the first guess $\rho_0(\theta)$. One may hope that a similar procedure could allow us to further improve the solution. Let us therefore consider the distance function

$$V(\theta) \equiv \frac{1}{2}\left(R(\theta) - \rho_1(\theta)\right)^2. \tag{5.1}$$

Taking the time derivative and factorizing as previously yield

$$\dot{V}(\theta) = -a(\theta)(R + \rho_2(\theta))(R - \rho_1(\theta))(R - \rho_2(\theta)), \tag{5.2}$$

where $\rho_2(\theta) > 0$ and $a(\theta) > 0$ are given by

$$\begin{aligned} \rho_2(\theta) &= \frac{2\ \left(1 + 4\ A^{3/2}\ \theta^{1/4}\right)^{3/4}\ \theta^{5/16}}{\sqrt{3\ A^{1/4} + 4\ A\ \left(1 + 4\ A^{3/2}\ \theta^{1/4}\right)^{3/2}\ \theta^{1/8} + 8\ A^{7/4}\ \theta^{1/4}}}, \\ a(\theta) &= \frac{3\ A^{1/4} + 4\ A\ \left(1 + 4\ A^{3/2}\ \theta^{1/4}\right)^{3/2}\ \theta^{1/8} + 8\ A^{7/4}\ \theta^{1/4}}{4\ R^2\ \left(1 + 4\ A^{3/2}\ \theta^{1/4}\right)^{3/2}\ \theta^{5/8}}. \end{aligned} \tag{5.3}$$

It can be shown that $\rho_2(\theta) > \rho_1(\theta)$ for all $\theta > 0$, which implies with (5.2) that

$$\begin{aligned} &\dot{V}(\theta) < 0 \text{ if } R > \rho_2(\theta) \text{ or } R < \rho_1(\theta), \\ &\dot{V}(\theta) > 0 \text{ if } \rho_1(\theta) < R < \rho_2(\theta); \end{aligned} \tag{5.4}$$

i.e., the crescent region bounded by the curves $R = \rho_1(\theta)$ and $R = \rho_2(\theta)$ is *attractive*. The situation is therefore similar to the previous case in the sense that we have identified another crescent-shaped region which is *attractive* for orbits that are outside this region. However, the arguments that we used in section 4 to prove that orbits entering this crescent are trapped no longer holds in this case. Indeed, the problem is that $\dot{\rho}_2 - \dot{\rho}_1 < 0$; i.e., the two curves get closer to each other as θ increases (which can be shown numerically for $A = 0.75$).

We cannot establish with the same argument that the orbit stays inside this new crescent, but we can at least claim that $\rho_2(\theta)$ is an asymptotic solution because $\rho_2(\theta) \sim \theta^{1/4}/\sqrt{A}$ as $\theta \to \infty$. We may ask if $\rho_2(\theta)$ is a better approximation of $R(\theta)$ than $\rho_1(\theta)$ for $0 \le \theta \le 1$. Numerical solutions (Figure 5.1) indicate that the orbits with $R_0 \approx 0$ are closer to $\rho_2(\theta)$ than to $\rho_1(\theta)$. In Figure 5.1, a low value of A was used to get a clearly visible spacing between the curves bounding the crescent. Indeed, for $A = 0.75$ the curves $\rho_1(\theta)$ and $\rho_2(\theta)$ are almost superposed. We can therefore propose the asymptotic solution

$$R(\theta) \sim \frac{2\ (1 + 4\ A^{3/2}\ \theta^{1/4})^{3/4}\ \theta^{5/16}}{\sqrt{3\ A^{1/4} + 4\ A\ (1 + 4\ A^{3/2}\ \theta^{1/4})^{3/2}\ \theta^{1/8} + 8\ A^{7/4}\ \theta^{1/4}}} \tag{5.5}$$

as $\theta \to \infty$, which is more accurate than $\rho_1(\theta)$ for $0 \le \theta \le 1$. As shown in Figure 5.2, $\rho_2(\theta)$ appears to be a good asymptotic solution. Moreover, the range of validity of $\rho_2(\theta)$ is broader if $R(0) \approx 0$, which is precisely the limit we are interested in.

Remark. The iterative process that allowed us to find $\rho_1(\theta)$ and $\rho_2(\theta)$, starting with $R = \rho_0(\theta)$, can be summarized as follows. In both cases, the new curve $R = \rho_{n+1}(\theta)$ bounding the crescent zone is the positive root of the equation

$$f(\rho_{n+1}, \theta) = \dot{\rho}_n(\theta), \tag{5.6}$$

where $\rho_n(\theta)$ is the previous curve. Using (2.23), (5.6) leads to the iteration formula

$$\rho_{n+1}(\theta) = \frac{\theta^{1/4}}{\sqrt{\sqrt{\theta}\ \dot{\rho}_n(\theta) + A}}. \tag{5.7}$$

Roughly speaking, (5.7) is a kind of *backward Picard iteration*, because we iterate a derivative instead of an integration. We notice that $\rho_n(0) = 0$ for all n and consequently the initial value $R(0) = 0$ is conserved exactly during iteration. Using the initial value $\dot{\rho}_{-1}(\theta) = 0$, we can iterate (5.7) to get successively $\rho_0(\theta)$, $\rho_1(\theta)$, and $\rho_2(\theta)$. It might be possible to generalize this iterative process to find asymptotic solutions for other ODEs.

6. Conclusions. The only *exact* result that we derived about the solution of the ODE (2.23) with $R(0) \approx 0$ is the functional form (3.9). Using (2.22), (3.9) leads to

$$x(\tau, p) = (p\ \tau)^{1/3}\ F(A\ p^{-1/3}\ \tau^{1/6}), \tag{6.1}$$

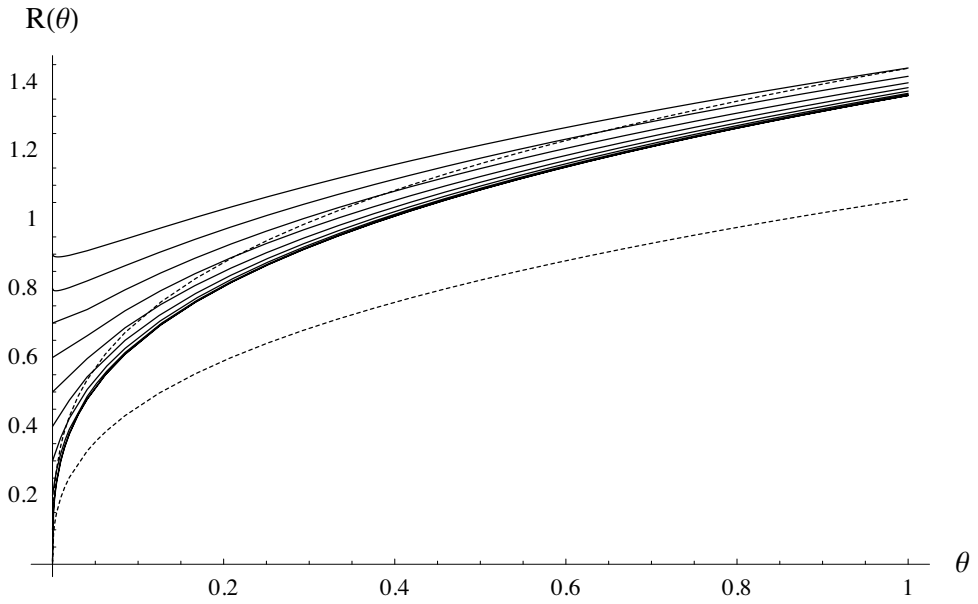

FIG. 5.1. *Results obtained with* $A = 0.1$. *The solid curves are numerical solutions obtained with* $R_0 = (0.01, 0.1, 0.2, 0.3, 0.4, 0.5, 0.6, 0.7, 0.8, 0.9)$. *Solutions with* $R_0 = 0.01,\ 0.1$ *are superposed. The dashed curves are* $R = \rho_1(\theta)$ *(bottom) and* $R = \rho_2(\theta)$ *(top). In the range* $0 \leq \theta \leq 1$, *orbits that enter the crescent remain in the crescent, move away from* $R = \rho_2(\theta)$ *as expected, but remain nevertheless closer to* $R = \rho_2(\theta)$ *than to* $R = \rho_1(\theta)$.

where F satisfies the ODE (3.10). Equation (6.1) could be useful to represent experimental data obtained with varying beam power p.

To compare the three approximate analytical solutions obtained in this paper, we plotted in Figure 6.1 (top) their relative errors (in percent) with respect to the numerical solution, using $A = 0.75$ and $R_0 = 0.001$. The perturbation solution (3.8) is the most accurate over most of the range, except for $\theta > 0.4$, where the asymptotic solution $R = \rho_2(\theta)$ is more accurate (using more terms in the perturbation solution would increase its accuracy). The asymptotic solution $R = \rho_2(\theta)$ is the second best approximation and its error has a minimum around $\theta = 0.004$. The third best approximation is $R = \rho_1(\theta)$.

The solution $R = \rho_1(\theta)$ is attractive because of its greatest simplicity. In spite of its slightly lower accuracy, we are going to see that this solution is the most useful in practice. First, we should first remember that the ODE studied in this paper is derived from an approximate model. In particular, the melt region is not exactly hemispherical and the model ODE is valid only for $\theta >> \theta_1 = 0.002$, for, say, $\theta \geq 0.02$. Knowing that experimental errors lie in the range of 5–10% [3], we can therefore conclude that the error in the approximate solutions of the model equations is smaller than the error in experimental measurement. From this standpoint, the most interesting solution is the one that offers a good compromise between simplicity and accuracy. From this perspective, the asymptotic solution $R(\theta) = \rho_1(\theta)$ is the simplest and has an error smaller than 3% in the validity range $\theta \geq 0.02$. More importantly, *this error decreases as* θ *increases*, which is not the case for the perturbation solution. To introduce explicitly the dependence on the beam power p, we can combine (2.24) and

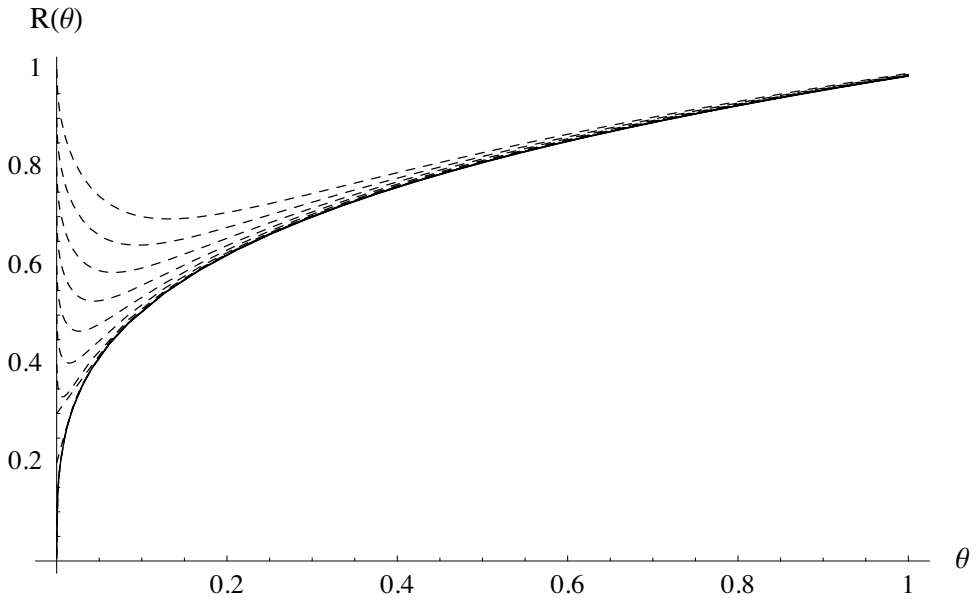

FIG. 5.2. *Results obtained with $A = 0.75$. The dashed curves are numerical solutions obtained with different positive values of $R(0) > 0$. The solid curve is the asymptotic solution $R = \rho_2(\theta)$.*

(4.3) to obtain

$$x(\tau, p) = \frac{2\ A^{1/4}\ p^{1/4}\ \tau^{3/8}}{\sqrt{1 + 4\ A^{3/2}\ p^{-1/2}\ \tau^{1/4}}}, \tag{6.2}$$

which gives an error smaller than 3% for $\tau \geq 12.5$, which corresponds to $t \geq 0.03\ \mu s$. A satisfactory comparison of the model (6.2) with experimental data is presented in [3].

We will conclude on a note about the geometrical method that we used to derive the asymptotic solution $R = \rho_1(\theta)$. This possibly original method leads us to three increasingly accurate asymptotic solutions $\rho_0(\theta)$, $\rho_1(\theta)$, and $\rho_2(\theta)$ that could be obtained by iterating the formula

$$f(\rho_{n+1}, \theta) = \frac{d}{d\theta}\ \rho_n(\theta) \tag{6.3}$$

starting with $\rho_{-1}(\theta) = 0$. In (6.3), f is the function that defines the ODE, i.e., $\frac{dR}{d\theta} = f(R, \theta)$. Roughly speaking, (6.3) is a kind of *backward Picard iteration*, because we iterate a derivative instead of an integration. It would be interesting to see if the iterative process (6.3) could be generalized to find approximate solutions for other ODEs.

Appendix A. Asymptotic behavior of $R(\theta)$ as $\theta \to 0$ for $A > 0$.

To study $R(\theta)$ around $\theta = 0$, we will make the hypothesis

$$R(\theta) \sim R_0 + c\ \theta^{\alpha} \tag{A.1}$$

as $\theta \to 0$, where $\alpha > 0$ and c is a constant. Substituting (A.1) into (2.23) yields

$$\frac{c\ \alpha}{\theta^{1-\alpha}} = -\frac{A}{\theta^{1/2}} + \frac{1}{(R_0 + c\ \theta^{\alpha})^2}. \tag{A.2}$$

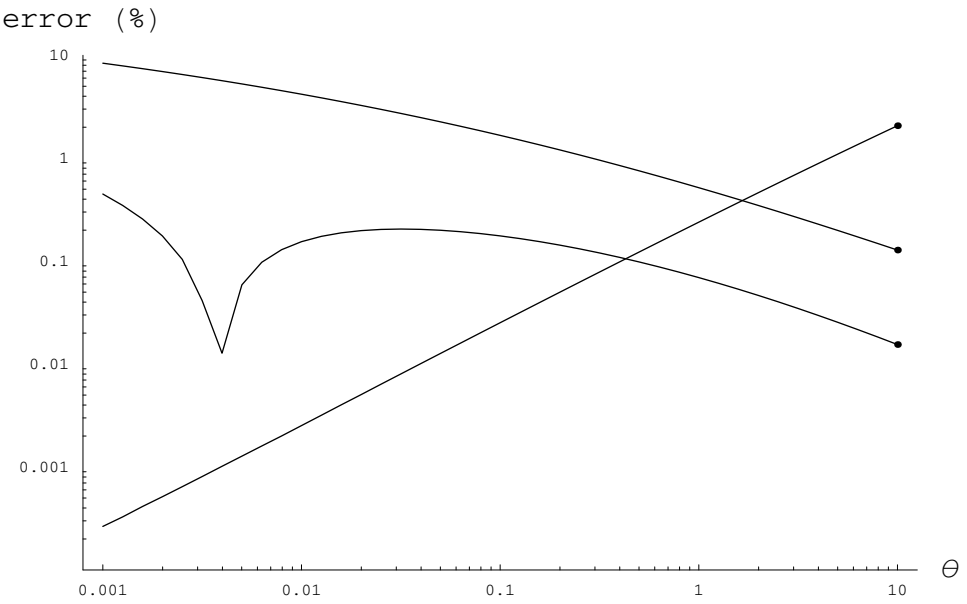

FIG. 6.1. *Comparison of the approximate solutions for* $A = 0.75$ *and* $R_0 = 0.001$. *We plotted the relative error in % with respect to the numerical solution, versus* θ. *Top-left: Error on* $R = \rho_1(\theta)$. *Center-left: Error on* $R = \rho_2(\theta)$. *Bottom-left: Error on the perturbation solution* (3.8).

If $R_0 > 0$, then the term $\frac{A}{\theta^{1/2}}$ on the right-hand side of (A.2) dominates as $\theta \to 0$. It follows that $c\ \alpha = -A$ and $1 - \alpha = 1/2 \Rightarrow \alpha = 1/2$, which in turn implies $c = -2A$. Hence, we have the asymptotic behavior

$$\text{If } R_0 > 0\ ,\ R(\theta) \sim R_0 - 2\ A\ \sqrt{\theta} \tag{A.3}$$

as $\theta \to 0$; i.e., *the orbit dives downward* before it eventually returns to an increasing regime. If $R_0 = 0$, (A.2) becomes

$$\frac{c\ \alpha}{\theta^{1-\alpha}} = -\frac{A}{\theta^{1/2}} + \frac{1}{c^2\ \theta^{2\alpha}}. \tag{A.4}$$

One must examine two cases. First, if we assume that $2\alpha > 1/2 \Rightarrow \alpha > 1/4$, then the term $1/(c^2\ \theta^{2\alpha})$ (right-hand side of (A.4)) dominates as $\theta \to 0$, and therefore $c\ \alpha = 1/c^2$ and $1 - \alpha = 2\ \alpha \Rightarrow \alpha = 1/3$, which also implies $c = 3^{1/3}$. Second, if we assume instead that $2\alpha < 1/2 \Rightarrow \alpha < 1/4$, then we must have $1 - \alpha = 1/2 \Rightarrow \alpha = 1/2$, which contradicts our assumption $\alpha < 1/4$. Hence, for $R_0 = 0$, we have the following asymptotic behavior:

$$\text{If } R_0 = 0,\ R(\theta) \sim (3\ \theta)^{1/3} \tag{A.5}$$

as $\theta \to 0$, which is consistent with (3.1).

Comparing (A.3) with (A.5), we see that solutions are qualitatively different for $R_0 > 0$ and $R_0 = 0$. Indeed, $R(\theta)$ *increases* if $R_0 = 0$, whereas it *decreases* if $R_0 > 0$. According to the DF, $R(\theta)$ should return rapidly to an increasing regime even if $R_0 > 0$. To see how this return occurs, we may try to find a better approximation of $R(\theta)$ around $\theta = 0$ with a MacLaurin expansion. Equation (3.5) implies that the derivatives of $R(s)$ are well defined at $s = 0$ as long as $R_0 > 0$, and therefore

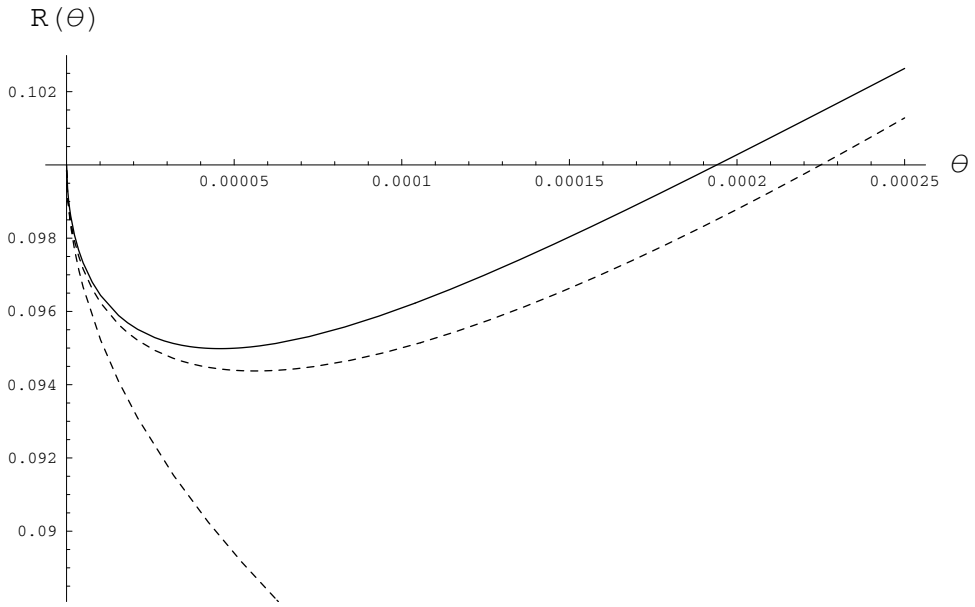

FIG. A.1. *Behavior of $R(\theta)$ around $\theta = 0$ for $R_0 = 0.1$. Here $A = 0.75$, and $\theta_{\min} \approx 0.000056$. The solid line is a numerical solution, and the dashed curves are $R_0 - 2\ A\ \sqrt{\theta}$ (going down) and $R_0 - 2\ A\ \sqrt{\theta} + \frac{1}{R_0^2}\ \theta$ (going back up).*

$R(s) = \sum_{n=0}^{\infty} \frac{1}{n!} \frac{d^n R}{ds^n}(0)\ s^n$. Using (3.5) to compute the derivatives $\frac{d^n R}{ds^n}(0)$ leads to $R(s) = R_0 - 2\ A\ s + \frac{s^2}{R_0^2} + \frac{8\ A}{3\ R_0^3}\ s^3 + (\frac{6\ A^2}{R_0^4} - \frac{1}{2\ R_0^5})\ s^4 + O(s)^5$, and replacing s by $\theta^{1/2}$ gives

$$R(\theta) = R_0 - 2\ A\ \theta^{1/2} + \frac{\theta}{R_0^2} + \frac{8\ A}{3\ R_0^3}\ \theta^{3/2} + O(\theta)^2. \tag{A.6}$$

The first three terms of (A.6) give the approximation $\tilde{R}(\theta) \equiv R_0 - 2\ A\ \theta^{1/2} + \frac{\theta}{R_0^2}$. The minimum of $\tilde{R}(\theta)$ occurs at $\theta_{\min} = A^2\ R_0^4$. As shown in Figure A.1, $\tilde{R}(\theta)$ describes fairly well the behavior of $R(\theta)$ around $\theta = 0$ for $R_0 > 0$.

Appendix B. Perturbation solution.

Substituting (3.7) into (2.23) yields

$$\sum_{n=0}^{\infty} A^n\ \dot{R}_n(\theta) = -\frac{A}{\sqrt{\theta}} + \frac{1}{(\sum_{n=0}^{\infty} A^n\ R_n(\theta))^2}. \tag{B.1}$$

Expanding the rightmost term of (B.1) in Taylor series around $A = 0$ to order 2 yields

$$\dot{R}_0 + \dot{R}_1\ A + \dot{R}_2\ A^2 = -\frac{A}{\sqrt{\theta}} + \frac{1}{R_0^2} - \frac{2}{R_0^3}\ R_1\ A + \left(\frac{3R_1^2}{R_0^4} - \frac{2}{R_0^3}\right)\ A^2, \tag{B.2}$$

where $\dot{f} \equiv \frac{df}{d\theta}$ for any function f. Identifying the terms of order 0, 1, and 2 yields

$$\begin{aligned} \dot{R}_0 &= \frac{1}{R_0^2}, \\ \dot{R}_1 &= -\frac{1}{\sqrt{\theta}} - \frac{2}{R_0^3}\, R_1, \\ \dot{R}_2 &= \frac{3R_1^2}{R_0^4} - \frac{2}{R_0^3}\, R_2. \end{aligned} \tag{B.3}$$

We will solve (B.3) with the initial value $R(0) = 0$. The solution of the first equation of (B.3) is $R_0(\theta) = (3\ \theta)^{1/3}$. Substituting $R_0(\theta)$ into the second equation of (B.3), we get

$$\dot{R}_1 + \frac{2}{3\ \theta}\, R_1 = -\frac{1}{\sqrt{\theta}}. \tag{B.4}$$

Fortunately, (B.4) is a nonhomogeneous *linear equation*. Its general solution is $R_1(\theta) = -\frac{6}{7}\ \sqrt{\theta} + \frac{\mathrm{C}}{\theta^{2/3}}$, where C is an arbitrary constant. The initial condition $R_1(0) = 0$ then imposes $\mathrm{C} = 0$ so that

$$R_1(\theta) = -\frac{6}{7}\ \sqrt{\theta}. \tag{B.5}$$

Using previous results for $R_0(\theta)$ and $R_1(\theta)$, the third equation of (B.3) becomes

$$\dot{R}_2 + \frac{2}{3\ \theta}\, R_2 = \frac{k_1}{\theta^{1/3}}, \tag{B.6}$$

where $k_1 = 4\ 3^{2/3}/49$, which is again a linear nonhomogeneous ODE. Its general solution is $R_2(\theta) = \frac{3}{49}\ (3\ \theta)^{2/3} + \frac{\mathrm{C}}{\theta^{2/3}}$, where C is an arbitrary constant. The initial condition $R_2(0) = 0$ again implies $\mathrm{C} = 0$, and therefore

$$R_2(\theta) = \frac{3}{49}\ (3\ \theta)^{2/3}. \tag{B.7}$$

This process can be continued, and the equations remain linear and easy to solve. The first six terms lead to the expansion (3.8).

Acknowledgments. We thank Christiane Rousseau, Pavel Winternitz, and Malidi Ahamadi for their comments on the early stages of this work. We also thank the anonymous referees for their subtle comments and constructive criticism.

REFERENCES

[1] D. Bäuerle, *Laser Processing and Chemistry*, 3rd ed., Springer-Verlag, Berlin, 2000.
[2] H. S. Carslaw and J. C. Jaeger, *Conduction of Heat in Solids*, Clarendon, Oxford, UK, 1988.
[3] J.-Y. Degorce, A. Saucier, and M. Meunier, *A simple analytical method for the characterization of the melt region of a semiconductor under a focused laser irradiation*, Appl. Surface Sci., 208–209 (2003), pp. 267–271.
[4] H. Kisdarjono, A. T. Voutsas, and R. Solanki, *Three-dimensional simulation of rapid melting and resolidification of thin Si films by excimer laser annealing*, J. Appl. Phys., 94 (2003), pp. 4374–4381.
[5] J. F. Ready and D. F. Farson, eds., *LIA Handbook of Laser Materials Processing*, Springer-Verlag, Berlin, 2001.

[6] R. K. Singh and J. Narayan, *Novel method for simulating laser-solid interactions in semiconductors*, Mat. Sci. Engrg., B3 (1989), pp. 217–230.
[7] V. N. Tokarev and A. F. H. Kaplan, *Modeling of time dependent pulsed laser melting*, J. Appl. Phys., 86 (1999), pp. 2836–2846.
[8] R. F. Wood and G. A. Geist, *Modeling of nonequilibrium melting and solidification in laser-irradiated materials*, Phys. Rev. B, 34 (1986), pp. 2606–2620.
[9] R. F. Wood and G. E. Giles, *Macroscopic theory of pulsed-laser annealing. I. Thermal transport and melting*, Phys. Rev. B, 23 (1981), pp. 2923–2942.